Insights into the Mechanism of Methanol Steam Reforming Tandem Reaction over CeO_2 Supported Single-site Catalysts

Luning Chen,[1,6,#] Zhiyuan Qi,[1,#] Xinxing Peng,[1] Jeng-Lung Chen,[5] Chih-Wen Pao,[5] Xibo Zhang,[6] Chaochao Dun,[2] Melissa Young,[4] David Prendergast,[2] Jeffrey J. Urban,[2] Jinghua Guo,[3] Gabor A. Somorjai[1,4,*] Ji Su,[1,2,*]

[1] Chemical Sciences Division, [2] Molecular Foundry, [3] Advanced Light Source, Lawrence Berkeley National Laboratory, Berkeley, California 94720, United States.

[4] Department of Chemistry, University of California-Berkeley, Berkeley, California 94720, United States.

[5] National Synchrotron Radiation Research Center, Science-Based Industrial Park Hsinchu 30076, Taiwan.

[6] State Key Laboratory of Physical Chemistry of Solid Surfaces, Collaborative Innovation Center of Chemistry for Energy Materials, and Department of Chemistry, College of Chemistry and Chemical Engineering, Xiamen University, Xiamen 361005, China.

Supporting Information Placeholder

ABSTRACT: We demonstrated the special synergy between noble metal single site and neighboring oxygen vacancies provided an “ensemble reaction pool” for high hydrogen generation efficiency and carbon dioxide (CO_2) selectivity of a tandem reaction, methanol steam reforming. Specifically, the hydrogen generation rate over single site Ru_1/CeO_2 catalyst is up to 9360 mol H_2 per mol Ru per hour (579 mL_{H2} g_{Ru}^{-1} s^{-1}) with 99.5 % CO_2 selectivity. Reaction mechanism study showed that the integration of metal single site and O vacancies facilitated the tandem reaction, which consisted of methanol dehydrogenation, water dissociation, and the subsequent water gas shift (WGS) reaction. In addition, the strength of CO adsorption and the reaction activation energy difference between methanol dehydrogenation and WGS reaction play an important role in determining the activity and CO_2 selectivity. Our study paves the way for the further rational design of single site catalysts at the atomic scale. Furthermore, the development of such highly efficient and selective hydrogen evolution systems promises to deliver highly desirable economic and ecological benefits.

INTRODUCTION

Single-site catalysts, where isolated metal atoms are anchored on supports by bonding to N or O atoms, have opened up a new research frontier in the catalysis field.[1-6] Downsizing metal nanoparticles to a single atom could achieve the maximum efficiency of utilizing noble metals and create more active sites.[7-11] Isolated metal sites typically show excellent activity in many catalytic reactions involving small molecules, such as CO oxidation, water gas shift (WGS) reaction, and methane selective oxidation.[12-14] However, the lack of ensemble sites prevents surface reactions that involve large molecules and some multi-step reactions.[15-17] Recent research demonstrated that “ensemble effects” between the metal single atoms and neighboring oxygen vacancies can favor the oxygen transfer and reactants adsorption, promoting the catalytic reaction efficiency with large molecules.[18-20] In our previous studies, we demonstrated the enhanced activity and selectivity of methanol dehydrogenation and n-hexane reforming when combining an oxygen vacancy with noble metal atoms.[21-23] The mechanism study also showed that the integration of metal single-sites and neighboring oxygen vacancies creates a special synergy that accelerates the reaction rates by facilitating the adsorption and activation of reactants and the transformation of intermediate species.[18,22] Therefore, we envisioned expanding the reaction scope to tandem reactions and study this “ensemble effect” of single-site catalysts further.

Moreover, hydrogen plays an important role in the transition to a cleaner energy landscape.[24] However, the safety of hydrogen transportation and storage remains a bottleneck for the upcoming hydrogen economy.[25,26] Storage hydrogen in chemical bonds of liquid organic hydrogen carriers (LOHCs) provides a possibility to overcome this limitation. Among all the LOHCs, methanol is identified as an ideal hydrogen carrier owing to its low cost and wide availability.[27] However, direct methanol dehydrogenation always co-produces CO, which will poison the catalysts, especially in the application of polymer electrolyte membrane fuel cells (PEMFCs).[28,29] On the other side, methanol steam reforming (MSR), as a tandem reaction,[30] consisting of two sequential reactions: methanol dehydrogenation ($CH_3OH = CO + 2\ H_2$) and water gas shift (WGS) reaction ($CO + H_2O = CO_2 + H_2$). Therefore, the total reaction of MSR ($CH_3OH + H_2O = CO_2 + 3\ H_2$) can not only avoid CO emissions but generate one more stoichiometrically equivalent hydrogen.[31] In the pioneering work, α-MoC supported single-site Pt or Ni catalysts were discovered exhibiting extraordinary hydrogen production activity in the aqueous-phase methanol reforming reaction.[32,33] The abundant surface hydroxyls of α-MoC provide highly active sites for water dissociation, thus accelerating the tandem methanol-reforming reaction at the interface between Pt_1 and α-MoC. However, the underlying tandem mechanism of MSR over single-site catalysts has remained elusive.

The tandem reactions catalyzed by functional nanostructures have been effectively studied.[34-37] Typically, tandem reactions occur on the multi-functional material surfaces or at the interface of different function materials.[34,38] Our previous mechanism studies of tandem reactions found the spatial arrangement of the interfaces of tandem catalyst could control the generation, diffusion and reaction of the intermediates and finally favor the selectivity of desired products.[39] However, single-site catalysts, the logical endpoint of the downsizing, have unique geometric and electronic structures. Therefore, the surface/interface reaction mechanism model that is suitable for traditional metal nanoparticle catalysts can no longer precisely describe the reaction behaviors occurring on the local environment of metal single-sites and need to be revamped. To further investigate the mechanism over these ensemble reaction sites, the key factor is to precisely control the spatial arrangement of the metal single-sites with oxygen vacancies.

In this work, we studied the mechanism of tandem MSR reaction over a series of CeO_2 supported single-site catalysts (Pt_1/CeO_2, Pd_1/CeO_2, Rh_1/CeO_2, Ru_1/CeO_2). We showed that well-defined reaction sites consisting of a metal single atom and neighboring oxygen vacancies possessed unique catalytic properties. Compared to the other three single-site catalysts, Ru_1/CeO_2 displayed the highest hydrogen production rate and CO_2 selectivity. Further study indicated that superior performance could be attributed to the synergy between the metal single site and neighboring oxygen vacancy.

EXPERIMENTAL METHODS

Synthesis of M_1/CeO_2 single-site catalysts (M = Ru, Rh, Pt, Pd).

Porous CeO_2 nanorods support was synthesized by following the previous report.[40] The single-site M_1/CeO_2 catalysts were synthesized by an ascorbic acid (AA)-assisted reduction method according to our prior work with some modifications.[20] Typically, 500 mg CeO_2 were first dispersed in 175 mL distilled water, and 1 mmol AA was added to the solution. After stirring at room temperature for 3 hours, the products were collected by centrifugation, washed with distilled water several times, and dried under vacuum, denoted as CeO_2-AA.

140 mg CeO_2-AA particles were then re-dispersed in 55 mL distilled water and 0.01 mmol metal precursor (H_2PtCl_6, $PdCl_2$, $RhCl_3$, $RuCl_3$) was added. After stirring for 3 hours at room temperature, the products were collected by centrifugation and washed with water several times. After dried under vacuum, the products were calcinated at 300 °C in the air for 5 hours to remove the excess AA, denoted as M_1/CeO_2.

Catalytic methanol steam reforming.

MSR over M_1/CeO_2 was performed in a continuous flow reactor. In a typical catalytic measurement, 100 mg catalysts were mixed with 500 mg white quartz (50-70 mesh particle size). Then the mixture was placed in a U-shaped fixed-bed flow reactor with an inner diameter of 4.50 mm, and the length of the catalyst bed is around 20 mm. Quartz wool was placed at both ends of the reactor. 30 mL/min helium, regulated by a mass flow controller, was fed to the reactor at 1 atm. Methanol/water mixture (3 mL/h) with varying ratios (pure methanol, 1:1, 1:3, 1:5) was fed into the reactor by an injection pump. A K-type thermocouple was fixed at the center of the catalyst, and the temperature of bed was controlled by a PID 697 controller. The products were analyzed online by HP 5890 GC (HayeSep D column) equipped with a TCD detector.

The conversion of methanol and selectivity of CO_2 were calculated by the following equations:

$$\text{Methanol Conversion } (\%) = \frac{\text{CO output} + \text{CO2 output}}{\text{Methanol input}} \times 100$$

$$\text{CO2 Selectivity } (\%) = \frac{\text{CO2 output}}{\text{CO output} + \text{CO2 output}} \times 100\%$$

Catalytic water gas shift (WGS) reaction.

The catalytic water gas shift (WGS) activities of M_1/CeO_2 catalysts were investigated using same catalyst amount in the same continuous flow reactor for MSR. 28 mL/min He and 2 mL/min CO were mixed and fed to the reactor at 1 atm, regulated by mass flow controllers. A flow of 2.25 mL/h of water was injected into the reactor. A K-type thermocouple was fixed in the center of catalysts and the temperature of the bed was controlled by a PID 697 controller. The products were analyzed online by HP 5890 GC (HayeSep D column) equipped with a TCD detector.

Further details are available in the Supporting Information.

RESULTS AND DISCUSSION

Synthesis and characterization of M_1/CeO_2 single-site catalysts.

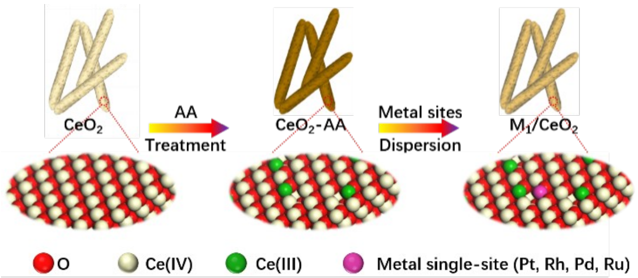

Scheme 1. Schematic presentation of the synthesis process for M_1/CeO_2 single-site catalysts (M = Pt, Rh, Pd, Ru).

Ru_1/CeO_2 were fabricated by an AA-assisted reduction route (Scheme 1). The ascorbic acid was first employed to create Ce^{3+} sites on the CeO_2 surface by reducing Ce^{4+}. Then, pre-reduced CeO_2-AA was dispersed in the solution. After adding ruthenium precursor ($RuCl_3$) solution, Ru was stabilized on the CeO_2 surface with the assistance of pre-reduced Ce^{3+} sites. After the calcination treatment in the air to remove the excess absorbed AA, the ruthenium single-sites were anchored on the CeO_2 support surface.

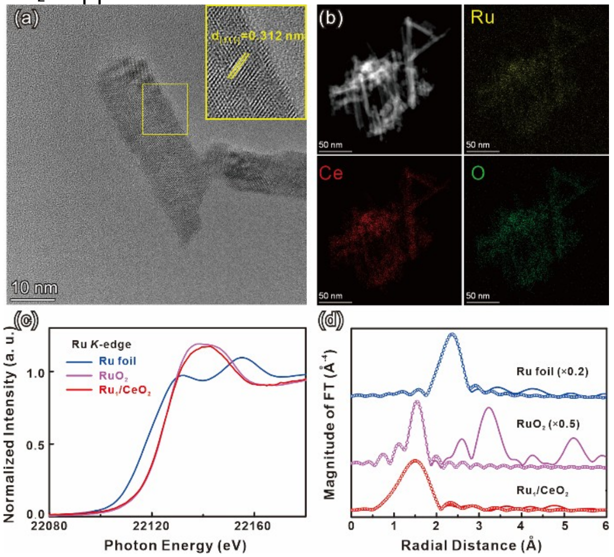

Figure 1. (a) High-resolution TEM image and (b) HAADF-STEM images and elemental mapping images of Ru_1/CeO_2 single-site catalyst. (c) Normalized XANES spectra of Ru_1/CeO_2, RuO_2, and bulk Ru foil at the Ru *K*-edge. (d) The k^3-weighted Fourier transform EXAFS spectra and the hollow points are fitting results.

Powder X-ray diffraction (XRD) and high-resolution transmission electron microscope (TEM) were employed to identify the Ru loading status on CeO_2. XRD patterns (Figure S1) show no additional peaks attributed to metallic Ru due to the low concentration of Ru and its single-site status. Besides, compared to the original CeO_2 support (Figure S2), no apparent Ru nanoparticles or clusters were observed (Figure 1a) while the signals of Ru are uniformly distributed throughout CeO_2, as shown in the element mapping (Figure 1b). Extended X-ray absorption fine structure (EXAFS) further confirmed the atomic dispersion of ruthenium. As shown in Figure 1d, only one notable peak attributed by Ru-O was observed in Fourier transformed (FT) k^3-weighted EXAFS spectrum while the Ru-Ru peak was not detected (Figure S3), indicating isolated Ru sites were atomically dispersed on CeO_2 (Detailed fitting parameters in Table S1).[41,42] Besides, the X-ray absorption near-edge structure (XANES) spectrum of Ru_1/CeO_2 suggested (Figure 1c) that Ru atoms carry a positive charge ($Ru^{\delta+}$) rather than Ru^0. This was further investigated by CO adsorption and desorption using *in situ* diffuse reflectance infrared Fourier transform spectroscopy (DRIFTS) (Figure S4). Four peaks at 2173, 2117, 2045, and 1975 cm^{-1} were detected, which is similar to those observed in other Ru single-site catalysts.[43,44] The peaks at 2045 and 1975 cm^{-1} are attributed to the pair of bands of dicarbonyl species of CO adsorbed on oxidized Ru sites, $Ru^{\delta+}(CO)_2$, while the peaks at 2173 and 2117 cm^{-1} are ascribed to monocaronyl species, $Ru^{\delta+}(CO)$, and tricarbonyl species, $Ru^{\delta+}(CO)_3$, respectively.

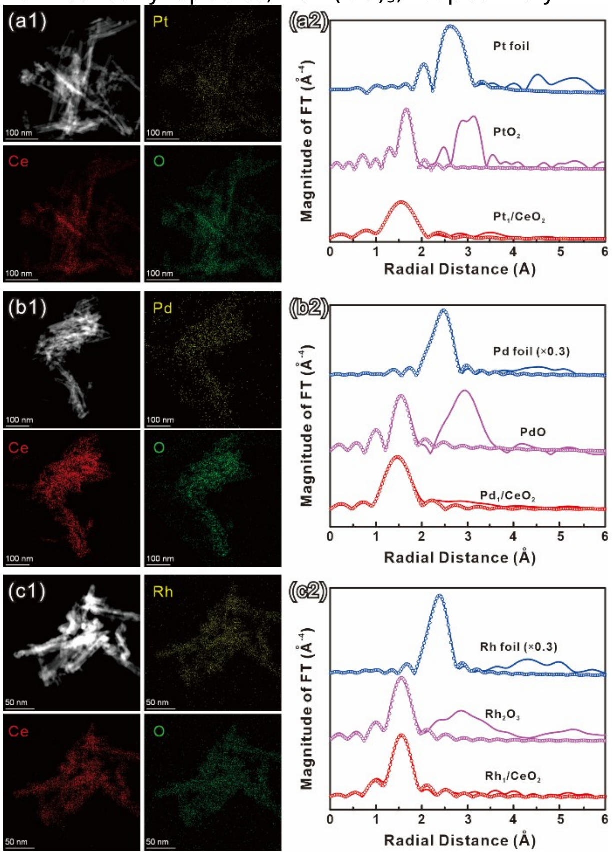

Figure 2. HAADF-STEM images and elemental mapping images of (a1) Pt_1/CeO_2, (b1) Pd_1/CeO_2 and (c1) Rh_1/CeO_2 single-site catalyst. (c) k^3-weighted Fourier transform EXAFS spectra of (a2) Pt_1/CeO_2, (b2) Pd_1/CeO_2, (c2) Rh_1/CeO_2 and their relative metal foil and metal oxides.

The AA-assisted method can be extended to fabricate various CeO_2 supported noble metal single-site catalysts (i.e. Pt, Pd, and Rh) by simply replacing $RuCl_3$ with other metal precursors like H_2PtCl_6, $PdCl_2$, or $RhCl_3$. As shown in Figure 2, the noble metal elements are all uniformly distributed on CeO_2 without any nanoparticles or clusters detected (Figure S5, The Corresponding energy spectra are listed in Figure S6). EXAFS spectra in Figure 2 show peaks contributed by the metal-oxygen bond, confirmed that the status of noble metal on CeO_2 are single sites. From the XANES spectrum (Figure S7-9), all the metal atoms are in the oxidized states rather than metallic states.

It has been reported that the introduction of noble metal single-sites (e.g., Au, Pd, Rh, and Ru) to CeO_2 can efficiently create oxygen vacancies near the dopant cations.[19,45-47] Combined theoretical calculation and spectrum measurement have proved that the generated oxygen vacancies are located near the metal single sites, which generated an ensemble reaction pool with the well-defined structure.[48] Synthetic methods such as atomic layer deposition (ALD) and impregnation-coprecipitation strategy would not involve the prereduction of the support, while our AA-assisted method can create more oxygen vacancies on the surface and thus have a higher chance to selectively immobilize metal single sites near the oxygen vacancy. According to XPS results (Figure S10, Table S2), the original proportion of Ce^{3+} in the shallow of as-synthesized CeO_2 is around 23.8%.[49] After AA reduction, the proportion of Ce^{3+} increased to 41.5%, indicating a lot of O vacancies were created on the surface, which agreed with electron paramagnetic resonance (EPR) spectra and Raman spectra (Figure S11, 12).[50,51] After air calcination to remove excess AA, the Ce^{3+} percentages of all M_1/CeO_2 decreased to a certain degree compared to CeO_2-AA, but they are still much higher than the original CeO_2 supports (Table S2). This result confirms the introduction of metal single sites could further stabilize the neighboring oxygen vacancies, which is consistent with the prior report.[52] Thus, more ensemble sites consisting of metal single site and surrounding oxygen vacancies were created via AA-assisted method, which could be potentially applied in multi-step tandem reactions.

Methanol reforming over Ru_1/CeO_2 single-site catalyst.

Compared to methanol dehydrogenation, MSR not only releases 3 H_2 per methanol by utilizing the H_2 from water, achieving a high H_2 gravimetric density of 18.8% but also avoids the generation of CO by the sequential WGS reaction.[31] Significantly, the gas products of methanol steam reforming are H_2 and CO_2, without the poisoning gas CO, which can be potentially applied in the polymer electrolyte membrane fuel cells (PEMFCs) without any pretretments.[32]

We first investigated the catalytic performance of Ru_1/CeO_2 in both methanol dehydrogenation and MSR reactions with different ratios of methanol and water. As shown in Figures 3a and 3c, methanol dehydrogenation (black line labeled as 1:0) starts at 150 °C, and the higher reaction temperature favors the methanol conversion. At 350 °C, the hydrogen production rate is 100.4 $mmol_{H2}\ g_{cat}^{-1}\ h^{-1}$ with a methanol conversion of 6.8%. The products of methanol dehydrogenation over Ru_1/CeO_2 only consist of H_2 and CO, and no formaldehyde was detected.

After introducing water vapor into the system, CO will further react with water through a sequential WGS reaction ($CO + H_2O = CO_2 + H_2$) over Ru_1/CeO_2. It will release one more H_2 and convert CO to CO_2. Compared to CO, CO_2 has a weaker bonding to the Ru single site, so it can be easily removed in the reaction condition, which will recover the active site for the next coming methanol and accelerate the reaction rate. Therefore, introducing water could enhance the H_2 production as well as the conversion of methanol (Figures 3a and 3c). Compared with pure methanol, feeding water and methanol vapor ($V_{methanol}/V_{water}$ = 1:1) together, the hydrogen generation rate increased to 207.6 $mmol_{H2}\ g_{cat}^{-1}\ h^{-1}$ at 350 °C, which is two times that of pure methanol. And 24.2% of methanol was converted, which is 4 folds of direct methanol dehydrogenation without water. The selectivity of CO_2 in the product is about 32.2% (Figure 3b) under the methanol and water ratio of 1:1.

Further increasing the water/methanol ratio to 3:1 leads to the methanol conversion of 25.6% and 97.8% selectivity of CO_2 at 350 °C, due to the enhanced WGS reaction facilitated by the excess water. As the feeding rate of water and methanol mixture is kept the same, less methanol was injected into the system. The lower methanol partial pressure decreases the generation rate of H_2 to 139.6 $mmol_{H2}\ g_{cat}^{-1}\ h^{-1}$, but still higher than that of the pure methanol (100.4 $mmol_{H2}\ g_{cat}^{-1}\ h^{-1}$). It also ranks the highest among the reported noble metal catalysts in terms of the CO_2 selectivity and H_2 generation rate (Figure S13). When compared with transition metal catalysts such as Cu/ZnO-based catalysts, Ru_1/CeO_2 also performed excellent activity and CO_2 selectivity in the temperature range of 150 °C to 350 °C (Table S3). Although the selectivity of CO_2 could increase to 99.5% at the water/methanol ratio of 5, the massive water vapor inhibited the methanol diffusion, leading to the lower H_2 generation rate of 23.8 $mmol_{H2}\ g_{cat}^{-1}\ h^{-1}$. Besides, at higher water concentrations (1:3 and 1:5), the relatively low methanol concentration will also slow down the growth of MSR rate at higher temperatures, because the methanol diffusion process was limited by a large amount of water molecules in the gas phase.

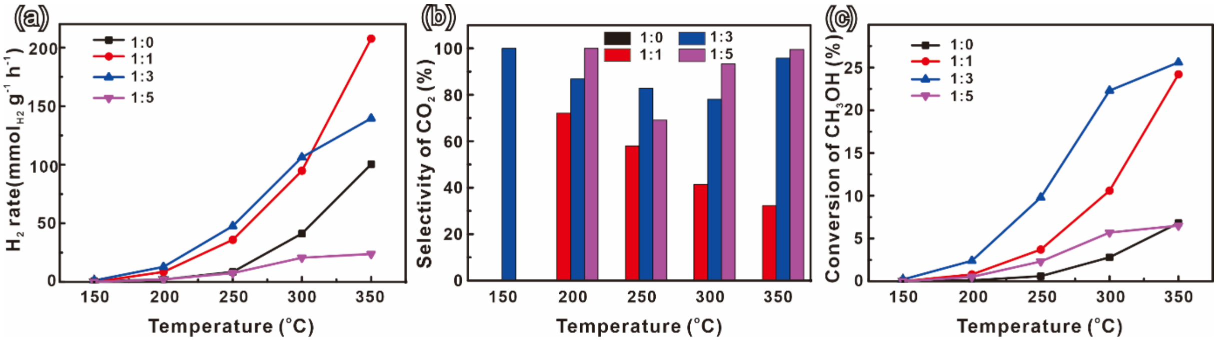

Figure 3. (a) Hydrogen generation rate (b) CO_2 selectivity and (c) methanol conversion of Ru_1/CeO_2 single-site catalyst at different temperatures with different ratios of methanol and water.

In practical application, the main issue hindering the application of single-site catalysts is their poor stability in the catalytic process, especially at operating temperature.[53] Therefore, the stability of Ru_1/CeO_2 was assessed in the catalytic reaction over time (Figure S14). The hydrogenation evolution rate was retained at 139.6 $mmol_{H2}$ g_{cat}^{-1} h^{-1} with more than 97% CO_2 selectivity within 72 hours testing of methanol steam reforming at 350 ℃ ($V_{methanol}/V_{water}$ = 1:3), indicating its excellent stability due to the strong interaction between Ru and CeO_2 surface.[54]

Methanol reforming on different M_1/CeO_2 single-site catalysts.

We further investigated the catalytic performance of MSR ($V_{methanol}/V_{water}$ = 1:3) over different M_1/CeO_2 catalysts (Ru_1/CeO_2, Rh_1/CeO_2, Pt_1/CeO_2, Pd_1/CeO_2) with a similar metal loading amount (0.14-0.15 wt. %). For Pt_1/CeO_2, Rh_1/CeO_2, and Pd_1/CeO_2, only a small number of products were detected above 200 ℃, of which the starting reaction temperature is higher than that of Ru_1/CeO_2 catalyst (150 ℃). Similar to Ru_1/CeO_2, higher temperature favors the reforming reaction rate (Figure 4a and 4c). Under the same reaction conditions and similar metal loading amount, Ru_1/CeO_2 showed the highest H_2 generation rate and methanol conversion with the activity order of Ru_1/CeO_2 > Rh_1/CeO_2 > Pt_1/CeO_2 > Pd_1/CeO_2.

More importantly, Ru_1/CeO_2 showed the highest CO_2 selectivity of 97.8% at 350 ℃, while the other three single-site catalysts have only less than 60 % CO_2 selectivity(Figure 4b). The catalytic results of MSR over M_1/CeO_2 showed that CO desorption and WGS are competing steps. Less CO desorption is the key to the higher selectivity of CO_2 in the subsequent WGS reaction. It has been reported that, compared with Pt, Rh, and Pd, Ru has the lowest CO adsorption energy both for bulk materials and single-atom, indicating Ru has a much stronger bonding of CO.[55,56] Therefore, CO-temperature-programmed desorption (CO-TPD) was then applied to investigate the strength of CO bonding on M_1/CeO_2 (Figure S15). The peak below 150 ℃ is attributed to CO adsorption on metal sites, while the peak between 200 ℃ to 300 ℃ is attributed to CO bonding on the CeO_2 support surface.[57,58] Notably, different from other metals, Ru_1/CeO_2, displays a CO desorption peak around 350 ℃, indicating the strong bonding between CO and Ru_1/CeO_2. In the reaction of methanol steam reforming, this strong interaction will further stabilize the CO intermediate species, providing more chance for subsequential WGS reaction. On the other side, the single site Pt, Pd, and Rh do not have this strong bonding at 350 ℃, so CO will desorb at lower temperatures, leading to the decreased CO_2 selectivity.

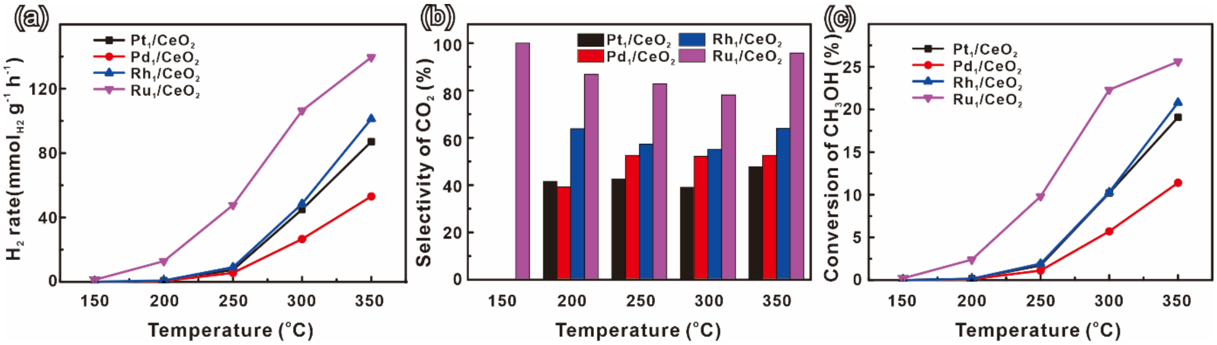

Figure 4. (a) Hydrogen generation rate (b) CO_2 selectivity and (c) methanol conversion of single-site M_1/CeO_2 catalysts at different temperatures with a 1:3 volume ratio of methanol and water.

Elementary-Step Methanol dehydrogenation and WGS Reaction.

MSR is a tandem reaction, including methanol dehydrogenation and subsequent WGS reaction. Therefore, we carried out methanol dehydrogenation and WGS reaction over M_1/CeO_2 separately. As shown in Figure 5a, the methanol dehydrogenation catalyzed by different M_1/CeO_2 shows various H_2 generation rates. Methanol starts to dehydrogenate over Rh_1/CeO_2 and Pt_1/CeO_2 at a lower temperature of 150 ℃, indicating the superior activity towards Ru_1/CeO_2 and Pd_1/CeO_2. The H_2 generation rates at 350 ℃ are in the order of Rh_1/CeO_2 (161.8 $mmol_{H2}$ g_{cat}^{-1} h^{-1}) > Pt_1/CeO_2 (152.9 $mmol_{H2}$ g_{cat}^{-1} h^{-1}) > Pd_1/CeO_2 (107.9 $mmol_{H2}$ g_{cat}^{-1} h^{-1}) > Ru_1/CeO_2 (100.4 $mmol_{H2}$ g_{cat}^{-1} h^{-1}). Interestingly, this activity trend is different from that of MSR in the presence of water, where H_2 generation rates are in the order of Ru_1/CeO_2 > Rh_1/CeO_2 > Pt_1/CeO_2 > Pd_1/CeO_2 (Figure 4a).

In the sequential WGS reaction (Figure 5c), Ru_1/CeO_2 has the highest activity from 200 to 350 ℃. Especially at a lower temperature (200 ℃), the CO conversion of Ru_1/CeO_2 (20.1%) is much higher than the other three catalysts, which are 7.5%, 0.9%, and 1.3% for Pt_1/CeO_2, Pd_1/CeO_2, Rh_1/CeO_2, respectively. The CO conversion of Ru_1/CeO_2 reached up to 100 % at the high temperature (350 ℃) while the WGS activity is in the order of Ru_1/CeO_2 > Pt_1/CeO_2 > Rh_1/CeO_2 > Pd_1/CeO_2.

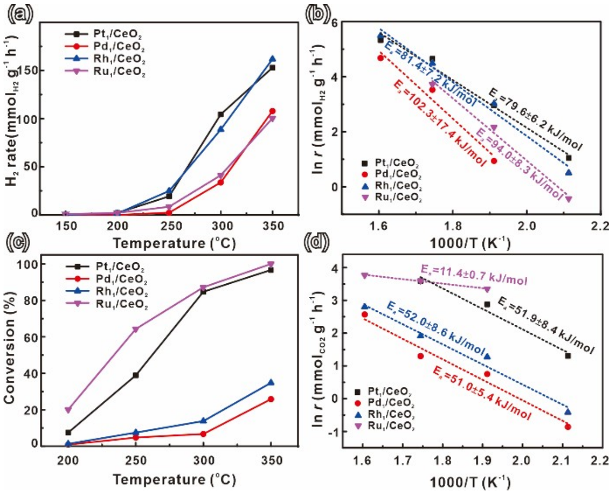

Figure 5. (a) H_2 generation rate over M_1/CeO_2 catalysts at different temperatures. (b) Arrhenius plots for methanol dehydrogenation over M_1/CeO_2 catalysts. (c) CO conversion of WGS over M_1/CeO_2 catalysts at different temperatures.

The apparent activation energy (E_a) is a well-known empirical parameter in chemical kinetics that characterizes the dependence of the chemical rate coefficients on the temperature and provides information to compare the intrinsic activity of the catalysts.[59] We thus calculated the apparent activation energies for both reactions (Figures 5b and 5d) to understand the reaction mechanism and chemical kinetics. The activation energy of methanol dehydrogenation (E_{a1}) is in the order of Pt_1/CeO_2 (79.6±6.2 kJ/mol) ≈ Rh_1/CeO_2 (81.4±7.2 kJ/mol) < Ru_1/CeO_2 (94.0±8.3 kJ/mol) < Pd_1/CeO_2 (102.3±17.4 kJ/mol), while the activation energy of WGS reaction (E_{a2}) is in the order of Ru_1/CeO_2 (11.4±0.7 kJ/mol) < Rh_1/CeO_2 (51.0±5.4 kJ/mol) ≈ Pt_1/CeO_2(51.9±8.4 kJ/mol) ≈ Pd_1/CeO_2 (52.0±8.6 kJ/mol). As reported, methanol steam reforming is a two-step reaction, where the activation energy of methanol dissociation (first step) is much higher than the subsequent WGS reaction (second step).[30] Meanwhile, the second step, WGS reaction, has a competing step, CO desorption. Therefore, the stronger CO adsorption and the lower E_{a2} of the WGS reaction could help the CO intermediates efficiently convert to CO_2 via the tandem reaction and recover more active sites for methanol dehydrogenation. Among all the studied single site catalysts, Ru_1/CeO_2 has an appropriate Ea_1 of methanol dehydrogenation, the lowest Ea_2 of WGS and the strongest CO adsorption, resulting in the highest H_2 production rate and CO_2 selectivity. On the contrary, Pt_1/CeO_2 has the lowest Ea_1, but its highest Ea_2 and weak bonding with CO, leading to the lowest CO_2 selectivity.

Proposed Reaction Mechanism.

Combined our experimental findings and the insights provided by the preceding work, we proposed a reaction mechanism of tandem MSR reaction over M_1/CeO_2. As shown in Scheme 2, the methanol dehydrogenation occurs on the metal single site to release hydrogen and form the intermediate CO, where the neighboring O vacancies will facilitate the dissociative adsorption of methanol.[22] Depending on the binding strength, CO_{ad} would either desorb from the active sites and ends with a low CO_2 selectivity (i.e., Pt_1/CeO_2 case), or directly react with water to yield CO_2 via the sequential WGS reaction. Dissociation of water is generally considered a key step in WGS,[60,61] and water molecules prefer to dissociate on the reduced CeO_x (O vacancy-Ce^{3+}) by transferring a H atom to the neighboring surface oxygen.[62,63] A recent study also revealed the synergistic effect between Pt sites and neighboring reduced Ce sites (Pt-O vacancy-Ce^{3+}) at the interface of the Pt clusters and the support,[64] and suggest only those oxygen vacancies nearby the Pt sites are involved in the WGS. M_1/CeO_2 in this work contains a similar structure, consisted of metal single sites with neighboring O vacancies (metal-O vacancy-Ce^{3+}). However, we could directly create much more "ensemble sites" using the AA-assisted synthetic approach, instead of a limited amount of active sites only at the interface of nanocluster and support, highlighting the great advantage of single-site catalysts. It has also been reported the introduction of metal heteroatoms could efficiently create oxygen vacancy next to the dopant cations. Therefore, in our proposed "ensemble reaction pool", the formed hydroxyl species adsorbed on the oxygen vacancy will react with the neighboring CO_{ad}, which avoids the diffusion process and lead to high activity.

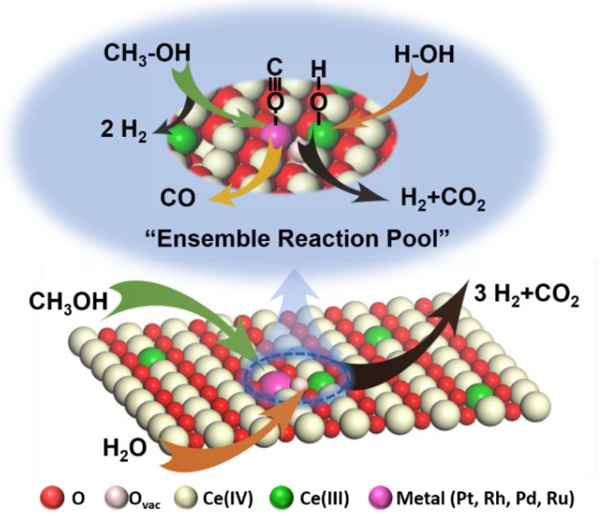

Scheme 2. Proposed reaction pathway for methanol steam reforming on M_1/CeO_2 single-site catalysts.

CONCLUSION

In summary, the mechanism of methanol steam reforming tandem reaction was investigated over a series of CeO_2 supported noble metal single site catalysts. Notably, Ru_1/CeO_2 displayed a much higher H_2 generation rate and CO_2 selectivity compared to the other three catalysts. Specifically, the stronger CO-metal bonding and larger difference of apparent activation energy between methanol dehydrogenation and WGS reaction resulted in its higher CO_2 selectivity. Importantly, different from metal nanoparticle catalyst, the metal single sites accompanied with neighboring O vacancies generate an "ensemble reaction pool" to combine the methanol dehydrogenation, water dissociation, and WGS reaction efficiently in the local environment. And this special synergy further improves the reaction efficiency and selectivity. Ultimately, this in-depth study highlights the benefits of well-designed single site catalysts for multiple steps catalysis and paves the way for further rational design based on the “ensemble reaction pool” concept.

ASSOCIATED CONTENT

Supporting Information

This material is available free of charge via the Internet at http://pubs.acs.org.

Experimental details, characterization data, and partial catalytic data, including the characterization of CeO_2 support, TEM images of M_1/CeO_2 catalyst, XPS spectra of CeO_2 and M_1/CeO_2, EPR and Raman spectra of CeO_2 and CeO_2-AA, CO adsorption-desorption DRIFTS of Ru_1/CeO_2, CO-TPD results of M_1/CeO_2 catalysts, stability test of Ru_1/CeO_2 catalyst.

AUTHOR INFORMATION

Corresponding Authors
* jisu@lbl.gov
* somorjai@berkeley.edu

Author Contributions

# L.C. and Z.Q. contributed equally to this work

Notes

The authors declare no competing financial interests.

ACKNOWLEDGMENT

This work was supported by the Hydrogen Materials Advanced Research Consortium (HyMARC), established as part of the Energy Materials Network by the U.S. Department of Energy, Office of Energy Efficiency and Renewable Energy, Fuel Cell Technologies Office, under Contract Number DE-AC02-05CH11231, and Director, Office of Basic Energy Sciences, Division of Chemical Sciences, Geological and Biosciences of the U.S. Department of Energy under the same contract. This research used resources of the Advanced Light Source, which is a DOE Office of Science User Facility under the same contract. J. Guo, D. Prendergast, C. Dun, J. Urban and J. Su were supported by a User Project at The Molecular Foundry at Lawrence Berkeley National Laboratory, which is supported by the Office of Science of the U.S. Department of Energy under the same contract. L. Chen and Z. Qi acknowledge the financial support provided by catalysis research program DOE/LBNL DE-AC02-05CH11231, FWP no. CH030201.

REFERENCES

(1) Kaiser, S. K.; Chen, Z.; Faust Akl, D.; Mitchell, S.; Pérez-Ramírez, J. Single-Atom Catalysts across the Periodic Table. *Chem. Rev.* **2020**, *120*, 11703-11809.

(2) Ji, S.; Chen, Y.; Wang, X.; Zhang, Z.; Wang, D.; Li, Y. Chemical synthesis of single atomic site catalysts. *Chem. Rev.* **2020**, *120*, 11900-11955.

(3) Lang, R.; Du, X.; Huang, Y.; Jiang, X.; Zhang, Q.; Guo, Y.; Liu, K.; Qiao, B.; Wang, A.; Zhang, T. Single-Atom Catalysts Based on the Metal-Oxide Interaction. *Chem. Rev.* **2020**, *120*, 11986-12043.

(4) Kistler, J.D.; Chotigkrai, N.; Xu, P.; Enderle, B.; Praserthdam, P.; Chen, C.Y.; Browning, N.D.; Gates, B.C. A single-site platinum CO oxidation catalyst in zeolite KLTL: microscopic and spectroscopic determination of the locations of the platinum atoms. *Angew. Chem. Int. Ed*. **2014**, *53*, 8904-8907.

(5) Rascón, F.; Wischert, R.; Copéret, C. Molecular nature of support effects in single-site heterogeneous catalysts: silica vs. alumina. *Chem. Sci.* **2011**, *2*, 1449-1456.

(6) Thomas, J.M.; Raja, R.; Lewis, D.W. Single-site heterogeneous catalysts. *Angew. Chem. Int. Ed*. **2005**, *44*, 6456-6482.

(7) Qiao, B.; Wang, A.; Yang, X.; Allard, L.F.; Jiang, Z.; Cui, Y.; Liu, J.; Li, J.; Zhang, T. Single-atom catalysis of CO oxidation using Pt_1/FeOx. *Nat. Chem.* **2011**, *3*, 634-641.

(8) Jones, J.; Xiong, H.; DeLaRiva, A.T.; Peterson, E.J.; Pham, H.; Challa, S.R.; Qi, G.; Oh, S.; Wiebenga, M.H.; Hernández, X.I.P.; Wang, Y. Thermally stable single-atom platinum-on-ceria catalysts via atom trapping. *Science*, **2016**, *353*, 150-154.

(9) Wang, L.; Zhang, W.; Wang, S.; Gao, Z.; Luo, Z.; Wang, X.; Zeng, R.; Li, A.; Li, H.; Wang, M.; Zheng, X. Atomic-level insights in optimizing reaction paths for hydroformylation reaction over Rh/CoO single-atom catalyst. *Nat. Comm.* **2016**, *7*, 1-8.

(10) Lee, B.H.; Park, S.; Kim, M.; Sinha, A.K.; Lee, S.C.; Jung, E.; Chang, W.J.; Lee, K.S.; Kim, J.H.; Cho, S.P.; Kim, H. Reversible and cooperative photoactivation of single-atom Cu/TiO_2 photocatalysts. *Nat. Mater.* **2019**, *18*, 620-626.

(11) Liu, P.; Zhao, Y.; Qin, R.; Mo, S.; Chen, G.; Gu, L.; Chevrier, D.M.; Zhang, P.; Guo, Q.; Zang, D.; Wu, B. Photochemical route for synthesizing atomically dispersed palladium catalysts. *Science* **2016**, *352*, 797-800.

(12) Nie, L.; Mei, D.; Xiong, H.; Peng, B.; Ren, Z.; Hernandez, X.I.P.; DeLaRiva, A.; Wang, M.; Engelhard, M.H.; Kovarik, L.; Datye, A.K. Activation of surface lattice oxygen in single-atom Pt/CeO_2 for low-temperature CO oxidation. *Science* **2017**, *358*, 1419-1423.

(13) Lin, J.; Wang, A.; Qiao, B.; Liu, X.; Yang, X.; Wang, X.; Liang, J.; Li, J.; Liu, J.; Zhang, T. Remarkable performance of Ir_1/FeOx single-atom catalyst in water gas shift reaction. *J. Am. Chem. Soc.* **2013**, *135*, 15314-15317.

(14) Shan, J.; Li, M.; Allard, L.F.; Lee, S.; Flytzani-Stephanopoulos, M. Mild oxidation of methane to methanol or acetic acid on supported isolated rhodium catalysts. *Nature* **2017**, *551*, 605-608.

(15) Jeong, H.; Kwon, O.; Kim, B.S.; Bae, J.; Shin, S.; Kim, H.E.; Kim, J.; Lee, H.; Highly durable metal ensemble catalysts with full dispersion for automotive applications beyond single-atom catalysts. *Nat. Catal.* **2020**, *3*, 368-375.

(16) Jeong, H.; Lee, G.; Kim, B.S.; Bae, J.; Han, J.W.; Lee, H. Fully dispersed Rh ensemble catalyst to enhance low-temperature activity. *J. Am. Chem. Soc.* **2018**, *140,* 9558-9565.

(17) Jeong, H.; Shin, S.; Lee, H. Heterogeneous Atomic Catalysts Overcoming the Limitations of

Single-Atom Catalysts. *ACS Nano* **2020**, *14*, 14355-14374.

(18) Wang, L.; Guan, E.; Zhang, J.; Yang, J.; Zhu, Y.; Han, Y.; Yang, M.; Cen, C.; Fu, G.; Gates, B.C.; Xiao, F.S. Single-site catalyst promoters accelerate metal-catalyzed nitroarene hydrogenation. *Nat. Comm.* **2018**, *9*, 1-8.

(19) Li, T.; Liu, F.; Tang, Y.; Li, L.; Miao, S.; Su, Y.; Zhang, J.; Huang, J.; Sun, H.; Haruta, M.; Wang, A. Maximizing the number of interfacial sites in single-atom catalysts for the highly selective, solvent-free oxidation of primary alcohols. *Angew. Chem. Int. Ed.* **2018**, *57*, 7795-7799.

(20) Yu, K.; Lou, L.L.; Liu, S.; Zhou, W. Asymmetric oxygen vacancies: the intrinsic redox active sites in metal oxide catalysts. *Adv. Sci.* **2020**, *7*, 1901970.

(21) Chen, L.N.; Hou, K.P.; Liu, Y.S.; Qi, Z.Y.; Zheng, Q.; Lu, Y.H.; Chen, J.Y.; Chen, J.L.; Pao, C.W.; Wang, S.B.; Li, Y.B. and *et. al.* Efficient hydrogen production from methanol using a single-site Pt_1/CeO_2 catalyst. *J. Am. Chem. Soc.* **2019**, *141*, 17995-17999.

(22) Qi, Z.; Chen, L.; Zhang, S.; Su, J.; Somorjai, G.A. Mechanism of Methanol Decomposition over Single-Site Pt_1/CeO_2 Catalyst: A DRIFTS Study. *J. Am. Chem. Soc.* **2021**, *143*, 60–64.

(23) Zhang, S.; Chen, L.; Qi, Z.; Zhuo, L.; Chen, J.L.; Pao, C.W.; Su, J.; Somorjai, G.A. Insights into the Mechanism of n-Hexane Reforming over a Single-Site Platinum Catalyst. *J. Am. Chem. Soc.* **2020**, *142*, 16533-16537.

(24) Tromp, T.K.; Shia, R.L.; Allen, M.; Eiler, J.M.; Yung, Y.L. Potential environmental impact of a hydrogen economy on the stratosphere. *Science* **2003**, *300*, 1740-1742.

(25) Muradov, N.Z.; Veziroğlu, T.N. "Green" path from fossil-based to hydrogen economy: an overview of carbon-neutral technologies. *Int. J. Hydrog. Energy*, **2008**, *33*, 6804-6839.

(26) Muradov, N.Z.; Veziroğlu, T.N. From hydrocarbon to hydrogen–carbon to hydrogen economy. *Int. J. Hydrog. Energy* **2005**, *30*, 225-237.

(27) Liu, W.C.; Baek, J.; Somorjai, G.A. The methanol economy: methane and carbon dioxide conversion. *Top. Catal.* **2018**, *61*, 530-541.

(28) Wang, T.; Chen, Z.X.; Yu, S.; Sheng, T.; Ma, H.B.; Chen, L.N.; Rauf, M.; Xia, H.P.; Zhou, Z.Y.; Sun, S.G. Constructing canopy-shaped molecular architectures to create local Pt surface sites with high tolerance to H_2S and CO for hydrogen electrooxidation. *Energy Environ. Sci.* **2018**, *11*, 166-171.

(29) Nilekar, A.U.; Sasaki, K.; Farberow, C.A.; Adzic, R.R.; Mavrikakis, M. Mixed-metal Pt monolayer electrocatalysts with improved CO tolerance. *J. Am. Chem. Soc.* **2011**, *133*, 18574-18576.

(30) Iulianelli, A.; Ribeirinha, P.; Mendes, A.; Basile, A. Methanol steam reforming for hydrogen generation via conventional and membrane reactors: a review. *Renew. Sust. Energ. Rev.* **2014**, *29*, 355-368.

(31) Palo, D.R.; Dagle, R.A.; Holladay, J.D. Methanol steam reforming for hydrogen production. *Chem. Rev.* **2017**, *107*, 3992-4021.

(32) Lin, L.; Zhou, W.; Gao, R.; Yao, S.; Zhang, X.; Xu, W.; Zheng, S.; Jiang, Z.; Yu, Q.; Li, Y.W.; Shi, C. Low-temperature hydrogen production from water and methanol using Pt/α-MoC catalysts. *Nature* **2017**, *544*, 80-83.

(33) Lin, L.; Yu, Q.; Peng, M.; Li, A.; Yao, S.; Tian, S.; Liu, X.; Li, A.; Jiang, Z.; Gao, R.; Han, X. and *et. al.* Atomically Dispersed Ni/α-MoC Catalyst for Hydrogen Production from Methanol/Water. *J. Am. Chem. Soc.* **2021**, 143, 1, 309–317

(34) Yamada, Y.; Tsung, C.K.; Huang, W.; Huo, Z.; Habas, S.E.; Soejima, T.; Aliaga, C.E.; Somorjai, G.A.; Yang, P. Nanocrystal bilayer for tandem catalysis. *Nature Chem.* 2011, *3*, 372-376.

(35) Rayder, T.M.; Adillon, E.H.; Byers, J.A.; Tsung, C.K. A Bioinspired Multicomponent Catalytic System for Converting Carbon Dioxide into Methanol Autocatalytically. *Chem*, **2020**, *6*, 1742-1754.

(36) Ma, H.; Ma, G.; Qi, Y.; Wang, Y.; Chen, Q.; Rout, K.R.; Fuglerud, T.; Chen, D. Nitrogen-Doped Carbon-Assisted One-pot Tandem Reaction for Vinyl Chloride Production via Ethylene Oxychlorination. *Angew. Chem. Int. Ed.* **2020**, *59*, 22080-22085.

(37) Cho, H.J.; Kim, D.; Li, J.; Su, D.; Xu, B. Zeolite-encapsulated Pt nanoparticles for tandem catalysis. *J. Am. Chem. Soc.* **2018**, *140*, 13514-13520.

(38) Chen, L.; Zhang, X.; Zhou, J.; Xie, Z.; Kuang, Q.; Zheng, L. A nano-reactor based on PtNi@ metal–organic framework composites loaded with polyoxometalates for hydrogenation–esterification tandem reactions. *Nanoscale* **2019**, *11*, 3292-3299.

(39) Su, J.; Xie, C.; Chen, C.; Yu, Y.; Kennedy, G.; Somorjai, G.A.; Yang, P. Insights into the mechanism of tandem alkene hydroformylation over a nanostructured catalyst with multiple interfaces. *J. Am. Chem. Soc*. **2016**, *138*, 11568-11574.

(40) Mai, H.X.; Sun, L.D.; Zhang, Y.W.; Si, R.; Feng, W.; Zhang, H.P.; Liu, H.C.; Yan, C.H. Shape-selective synthesis and oxygen storage behavior of ceria nanopolyhedra, nanorods, and nanocubes. *J. Phys. Chem. B.* **2005**, *109*, 24380-24385.

(41) Ravel, B.; Newville, M.A.T.H.E.N.A. ATHENA, ARTEMIS, HEPHAESTUS: data analysis for X-ray absorption spectroscopy using IFEFFIT. *J. Synchrotron Radiat.* **2005**, *12*, 537-541.

(42) Sarma, B.B.; Kim, J.; Amsler, J.; Agostini, G.; Weidenthaler, C.; Pfänder, N.; Arenal, R.; Concepción, P.; Plessow, P.; Studt, F.; Prieto, G. One-pot cooperation of single-atom Rh and Ru solid catalysts for a selective tandem olefin isomerization-hydrosilylation process. *Angew. Chem. Int. Ed.* **2020**, *59*, 5806-5815.

(43) Thang, H.V.; Tosoni, S.; Fang, L.; Bruijnincx, P.; Pacchioni, G. Nature of Sintering-Resistant, Single-Atom Ru Species Dispersed on Zirconia-Based Catalysts: A DFT and FTIR Study of CO Adsorption. *ChemCatChem* **2018**, *10*, 2634-2645.

(44) Qiu, J.Z.; Hu, J.; Lan, J.; Wang, L.F.; Fu, G.; Xiao, R.; Ge, B.; Jiang, J. Pure Siliceous Zeolite-Supported Ru Single-Atom Active Sites for Ammonia Synthesis. *Chem. Mater.* **2019**, *31*, 9413-9421.

(45) Fu, Q.; Saltsburg, H.; Flytzani-Stephanopoulos, M. Active nonmetallic Au and Pt species on ceria-based water-gas shift catalysts. *Science* **2013**, *301*, 935-938.

(46) Shapovalov, V.; Metiu, H. Catalysis by doped oxides: CO oxidation by $Au_xCe_{1-x}O_2$. *J. Catal.* **2017**, *245*, 205-214.

(47) Tang, W.; Hu, Z.; Wang, M.; Stucky, G.D.; Metiu, H.; McFarland, E.W. Methane complete and partial oxidation catalyzed by Pt-doped CeO_2. *J. Catal.* **2010***, 273*, 125-137.

(48) Liu, C.; Chen, Z.; Yan, H.; Xi, S.; Yam, K.M.; Gao, J.; Du, Y.; Li, J.; Zhao, X.; Xie, K.; Xu, H. Expedient synthesis of E-hydrazone esters and 1H-indazole scaffolds through heterogeneous single-atom platinum catalysis. *Sci. Adv.* **2019**, *5*, 1537.

(49) Chen, J.; Wanyan, Y.; Zeng, J.; Fang, H.; Li, Z.; Dong, Y.; Qin, R.; Wu, C.; Liu, D.; Wang, M.; Kuang, Q.; Xie, Z.; Zheng, L. Surface engineering protocol to obtain an atomically dispersed Pt/CeO_2 catalyst with high activity and stability for CO oxidation. *ACS Sustain. Chem. Eng.* **2018**. *6*, 14054-14062.

(50) Khan, M.E.; Khan, M.M.; Cho, M.H. Ce^{3+}-ion, surface oxygen vacancy, and visible light-induced photocatalytic dye degradation and photocapacitive performance of CeO_2-graphene nanostructures. *Sci. Rep.* **2017**, 7, 1-17.

(51) Lykaki, M.; Pachatouridou, E.; Carabineiro, S.A.; Iliopoulou, E.; Andriopoulou, C.; Kallithrakas-Kontos, N.; Boghosian, S.; Konsolakis, M. Ceria nanoparticles shape effects on the structural defects and surface chemistry: Implications in CO oxidation by Cu/CeO_2 catalysts. *Appl. Catal. B*. **2018**, *230*, 18-28.

(52) McFarland, E.W.; Metiu, H. Catalysis by doped oxides. *Chem. Rev.* **2013**, *113*, 4391-4427.

(53) Duan, S.; Wang, R.; Liu, J. Stability investigation of a high number density Pt_1/Fe_2O_3 single-atom catalyst under different gas environments by HAADF-STEM. *Nanotechnology* **2018**, *29*, 204002.

(54) Liu, J.C.; Tang, Y.; Wang, Y.G.; Zhang, T.; Li, J. Theoretical understanding of the stability of single-atom catalysts. *Natl. Sci. Rev.* **2018***, 5*, 638-641.

(55) Abild-Pedersen, F.; Andersson, M.P. CO adsorption energies on metals with correction for high coordination adsorption sites–A density functional study. *Surf. Sci.* **2017**, *601*, 1747-1753.

(56) Sarma, B.B.; Plessow, P.N.; Agostini, G.; Concepción, P.; Pfänder, N.; Kang, L.; Wang, F.R.; Studt, F.; Prieto, G. Metal-specific reactivity in single-atom catalysts: CO oxidation on 4d and 5d transition metals atomically dispersed on MgO. *J. Am. Chem. Soc.* **2020**, *142*, 14890-14902.

(57) Wu, Z.; Li, M.; Overbury, S. H. On the Structure Dependence of CO Oxidation over CeO_2 nanocrystals with Well-Defined Surface Planes. *J. Catal.* **2012**, *285*, 61-73

(58) Zhu, H. O.; Kim, J. R.; Ihm, S. K. Characteristics of Pt/WO_3/CeO_2/ZrO_2 Catalysts for Catalytic Reduction of NO by CO. *Appl. Catal. B* **2009**, *86*, 87-92.

(59) Calderón-Cárdenas, A.; Paredes-Salazar, E.A.; Varela, H. Apparent Activation Energy in Electrochemical Multistep Reactions: A Description via Sensitivities and Degrees of Rate Control. *ACS Catal.* **2020**, *10*, 9336-9345.

(60) Song, W.; Hensen, E.J. Mechanistic aspects of the water–gas shift reaction on isolated and clustered Au atoms on CeO_2 (110): A density functional theory study. *ACS Catal.* **2014**, *4*, 1885-1892.

(61) Vecchietti, J.; Bonivardi, A.; Xu, W.; Stacchiola, D.; Delgado, J.J.; Calatayud, M.; Collins, S.E. Understanding the role of oxygen vacancies in the water gas shift reaction on ceria-supported platinum catalysts. *ACS Catal.* **2014***, 4*, 2088-2096.

(62) Vovchok, D.; Guild, C.J.; Dissanayake, S.; Llorca, J.; Stavitski, E.; Liu, Z.; Palomino, R.M.; Waluyo, I.; Li, Y.; Frenkel, A.I.; Rodriguez, J.A. In situ characterization of mesoporous Co/CeO_2 catalysts for the high-temperature water-gas shift. *J. Phys. Chem. C*, **2018**, *122*, 8998-9008.

(63) Aranifard, S.; Ammal, S.C.; Heyden, A. On the importance of metal–oxide interface sites for the water–gas shift reaction over Pt/CeO_2 catalysts. *J. Catal.* **2014**, *309*, 314-324.

(64) Li, Y.; Kottwitz, M.; Vincent, J.L.; Enright, M.J.; Liu, Z.; Zhang, L.; Huang, J.; Senanayake, S.D.; Yang, W.C.D.; Crozier, P.A.; Nuzzo, R.G. Dynamic structure of active sites in ceria-supported Pt catalysts for the water gas shift reaction. *Nat. Comm.* **2021**, *12*, 1-9.

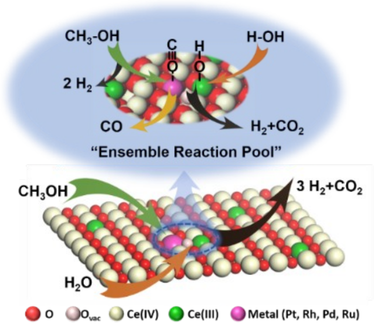
CH$_3$-OH
C
O
H
O
H-OH
2 H$_2$
CO
H$_2$+CO$_2$
"Ensemble Reaction Pool"
CH$_3$OH
3 H$_2$+CO$_2$
H$_2$O
O
O$_{vac}$
Ce(IV)
Ce(III)
Metal (Pt, Rh, Pd, Ru)